

UC Berkeley

UC Berkeley Previously Published Works

Title

Tailoring the Redox Reactions for High-Capacity Cycling of Cation-Disordered Rocksalt Cathodes

Permalink

<https://escholarship.org/uc/item/865295qh>

Journal

Advanced Functional Materials, 31(14)

ISSN

1616-301X

Authors

Yue, Yuan
Li, Ning
Ha, Yang
[et al.](#)

Publication Date

2021-04-01

DOI

10.1002/adfm.202008696

Peer reviewed

Tailoring the Redox Reactions for High-Capacity Cycling of Cation-Disordered Rocksalt Cathodes

Yuan Yue,¹ Ning Li,¹ Yang Ha,² Matthew J. Crafton,³ Bryan D. McCloskey,^{1,3} Wanli Yang,^{2,*} and Wei Tong^{1,*}

¹*Energy Storage and Distributed Resources Division, Lawrence Berkeley National Laboratory, Berkeley, CA 94720 USA*

²*Advanced Light Source, Lawrence Berkeley National Laboratory, Berkeley, CA 94720 USA*

³*Department of Chemical and Biomolecular Engineering, University of California, Berkeley, CA 94720, USA*

**Correspondence: weitong@lbl.gov, wlyang@lbl.gov*

Abstract

Cation-disordered rocksalts (DRXs) have emerged as a new class of high-capacity Li-ion cathode materials. One unique advantage of the DRX chemistry is the structural flexibility that substantially lessens the elemental constraints in the crystal lattice, such as Li content, choice of transition metal redox center paired with appropriate d^0 metal, and incorporation of F anion, which allows the optimization of the key redox reactions. Herein, a series of the DRX oxyfluorides based on the Mn redox have been designed and synthesized. By tailoring the stoichiometry of the DRX compositions, we have successfully demonstrated the high-capacity cycling by promoting the cationic $\text{Mn}^{2+}/\text{Mn}^{4+}$ redox reactions while suppressing those from anionic O. A highly fluorinated DRX compound, $\text{Li}_{1.2}\text{Mn}_{0.625}\text{Nb}_{0.175}\text{O}_{1.325}\text{F}_{0.675}$ ($\text{M}_{0.625}\text{F}_{0.675}$), delivers a capacity of ~ 170 mAh g^{-1} at C/3 for 100 cycles. This work showcases the concept of

balancing the cationic and anionic redox reactions in the DRX cathodes for improved electrochemical performance through the rational composition design.

1. Introduction

Novel cathode materials with higher capacity and energy density as well as longer cycle life are critical to the advancement of lithium-ion batteries.^[1] Recent discovery of a new class of Li-excess cation-disordered rocksalts (DRXs) has aroused significant interests in the development of alternative Co-free cathodes based on the earth-abundant and inexpensive transitional metals (TMs) such as Mn.^[2] Previous studies have established the fundamental principle of the Li⁺ percolation in the DRX lattice, which becomes feasible between two octahedral (*o*) sites through an intermediate tetrahedral (*t*) site (*o-t-o* diffusion) with a critical amount of Li excess ($\geq 9\%$).

[2a, 3]

Typical DRX cathodes can deliver a high capacity ($>250 \text{ mAh g}^{-1}$) that involves both cationic TM redox and anionic O redox processes.^[4] Despite the additional capacity contributed by anionic O redox, oxygen oxidation reaction typically occurs at high voltages.^[5] The co-existence of the oxidized oxygen and highly oxidized TM cations along with the organic solvents often triggers the complex parasitic reactions at high voltages, resulting in gas evolution and solid electrolyte interphase (SEI) formation. These irreversible reactions mostly take place at the surface, leading to surface densification with local Li deficiency, which deteriorates the Li⁺ diffusion pathway and manifests itself negatively as the gradual capacity loss during cycling.^[6]

A potential strategy to mitigate the negative impacts of the parasitic side reactions associated with anionic O redox at high voltages is to optimize the key redox reactions in the DRX cathodes. It has been demonstrated fluorinating DRX cathodes by substituting fluorine for oxygen can effectively enhance the cationic redox reactions and suppress oxygen release.^[7] Of

note, for a given oxide formula, replacing O^{2-} by less negatively charged F^- requires to lower the total positive charge of cations in $Li_{1+a}M_bM'_{1-a-b}O_{2-z}F_z$ (M is redox active metal, M' is charge compensator), therefore, enabling an increased stoichiometry of less positively charged cation, which is typically the low-valence redox active metal (e.g., $M = Mn$ or Ni) rather than the high-valence charge compensating d^0 metals (e.g., $M' = Nb, Mo, Ti, \text{etc.}$). At a fixed Li content, this means the possibility to tailor the cationic and anionic oxidation reactions.^[5g, 6d, 8] Alternatively, introducing the multi-valence cation allows more Li^+ transport per TM redox center, thus reduces the available Li^+ to accommodate the reactions associated with anionic oxygen at high voltages.^[9]

Guided by the similar design principle, highly fluorinated DRX cathodes based on the redox centers of Mn^{2+} (i.e., $Li_{1.333}Mn_{0.444}Nb_{0.222}O_{1.333}F_{0.667}$ and $Li_{1.333}Mn_{0.333}Ti_{0.333}O_{1.333}F_{0.667}$)^[9a] or mixed Mn^{2+}/Mn^{3+} (i.e., $Li_{1.25}Mn(II)_{0.167}Mn(III)_{0.583}O_{1.33}F_{0.67}$)^[7b] have been prepared to verify the reversibility of the Mn^{2+}/Mn^{4+} redox. Indeed, the structural flexibility of DRX materials allows a relatively wide range of Li and TM stoichiometry (or Li/TM ratio).^[7a, 10] It is well known that the theoretical capacity depends on both the extractable Li^+ and accessible redox reactions. With the reservoir of oxygen redox in these materials, a high Li content principally facilitates more oxygen oxidation during charge. For example, with 1.333 Li^+ in $Li_{1.333}Mn_{0.444}Nb_{0.222}O_{1.333}F_{0.667}$, 0.888 Li^+ extraction/insertion can be achieved based on Mn^{2+}/Mn^{4+} redox, leaving 0.445 Li^+ potentially available for oxygen oxidation.

In this work, we design new compositions to balance the use of reversible Mn^{2+}/Mn^{4+} redox with accessible Li^+ in the DRX materials. Herein, a series of Li-Mn²⁺-Nb⁵⁺-O-F DRX compositions, $Li_{1.2}Mn_{0.4+z/3}Nb_{0.4-z/3}O_{2-z}F_z$, are designed with a fixed Li content of 1.2, which remains in the critical Li excess range to warrant an efficient Li^+ percolation. By varying the F content, $z = 0.15, 0.3, 0.45, 0.6, \text{ and } 0.675$, the electrochemical properties of these DRX

materials are scrutinized, especially on the use of cationic $\text{Mn}^{2+}/\text{Mn}^{4+}$ redox. We demonstrate the stable cycling of high-capacity DRX cathode, mostly based on $\text{Mn}^{2+}/\text{Mn}^{4+}$ redox, at a reasonably high rate. These results demonstrates an effective strategy for the design of high-performance DRX cathodes for the high-capacity and stable-cycling Li-ion batteries.

2. Results

2.1 Material Design and Synthesis

To manipulate the cationic redox via fluorine substitution, the Li content is fixed at 1.2 per formula unit, a range of F contents from 0.15 to 0.3, 0.45, 0.6, and 0.675 are designed. To achieve the charge balance, the Mn^{2+} index is 0.45, 0.5, 0.55, 0.6, and 0.625, respectively. The resulting samples are labelled by Mn and F content, for example, $\text{M}_{0.45}\text{F}_{0.15}$ represents $\text{Li}_{1.2}\text{Mn}_{0.45}\text{Nb}_{0.35}\text{O}_{1.85}\text{F}_{0.15}$. The theoretical capacities based on $\text{Mn}^{2+}/\text{Mn}^{4+}$ redox and total 1.2 Li^+ are presented in **Figure 1a**, showing more theoretical capacity from the $\text{Mn}^{2+}/\text{Mn}^{4+}$ redox with increasing F content, while the total capacity based on all 1.2 Li^+ mostly remains similar for all the designed compositions, given the similar molecular weight. The theoretical calculation clearly shows that a much greater capacity can be achieved based on cationic Mn redox in highly fluorinated samples. For example, the Mn redox can theoretically compensate for all the capacity based on 1.2 Li^+ in $\text{M}_{0.60}\text{F}_{0.60}$ sample ($\text{Li}_{1.2}\text{Mn}_{0.6}\text{Nb}_{0.2}\text{O}_{1.4}\text{F}_{0.6}$). We demonstrate that it is possible to obtain the cubic DRX phase via a mechanochemical reaction, despite the general trend that highly fluorinated DRX samples require longer milling. The optimal milling time for each material is presented in **Figure S1**. The X-ray diffraction (XRD) patterns (**Figure 1b**) of the final products share the common cubic rocksalt features of $Fm\bar{3}m$ (**Figure 1d**). The broad reflections are due to the nanosized crystallites after the extended mechanical milling.^[2b] As shown in

Figure 1b, all the reflections show a slight shift towards the high 2θ value with increasing F content, indicating the decrease of lattice parameter. Rietveld analysis is performed on all the XRD patterns (**Figure S1**) and the detailed refinement results are listed in **Table S1**. We plot the lattice parameter as a function of TM and O/F content in these DRX compounds (**Figure 1c**). The smaller lattice parameter of the highly fluorinated samples is attributed to the increased amount of smaller Mn^{2+} cation (0.81 Å) and F^- anion (1.19 Å) compared to Nb^{5+} (0.86 Å) and O^{2-} (1.26 Å), respectively. The as-produced DRX materials are composed of the agglomerated secondary particles of a few micrometers (**Figure S2**) and X-ray energy dispersive spectroscopy (EDS) maps reveal the uniform distribution of Mn, Nb, O and F in the final products (**Figure S3**).

2.2 Electrochemical Characterization

The as-synthesized $\text{Li}_{1.2}\text{Mn}_{0.4+z/3}\text{Nb}_{0.4-z/3}\text{O}_{2-z}\text{F}_z$ samples were subjected to galvanostatic charge and discharge cycling tests. All the DRX samples deliver a reversible capacity of 250 – 300 mAh g^{-1} , corresponding to 0.9 – 1 Li^+ per formula unit (**Figure 2a**). Meanwhile, they exhibit similar sloping profiles on discharge, however, a small variation in the high-voltage region during charge is noticed. With increasing F and Mn^{2+} content, the plateau around 4.5 V diminishes. It has been known that this high-voltage plateau is related to the lattice oxygen oxidation.^[11] Here, the diminishing plateau seems in good accordance with the excellent cyclability of the highly fluorinated DRX sample (**Figure 2b**). In comparison, $\text{Li}_{1.2}\text{Mn}_{0.625}\text{Nb}_{0.175}\text{O}_{1.325}\text{F}_{0.675}$ ($\text{M}_{0.625}\text{F}_{0.675}$) displays an initial discharge capacity of 258 mAh g^{-1} , with 242 mAh g^{-1} maintained after 20 cycles, corresponding to 93.8% capacity retention. While at a low F content, $\text{Li}_{1.2}\text{Mn}_{0.45}\text{Nb}_{0.35}\text{O}_{1.85}\text{F}_{0.15}$ ($\text{M}_{0.45}\text{F}_{0.15}$) delivers a discharge capacity of 294 and 166 mAh g^{-1} during

the 1st and 20th cycle, respectively, corresponding to a capacity retention of 56.5%. Note that the greater discharge capacity at less fluorination (less Mn) suggests oxygen redox is more prone to participate in less fluorinated samples, meanwhile, the fluorination likely affects the Li⁺ extractability, and it is possible Li⁺ becomes more difficult to be extracted with the presence of more electronegative F⁻. Upon cycling, the capacity decay in less fluorinated samples is consistent with the loss of the high-voltage charge plateau and polarization buildup (**Figure 2c** & **Figure S4**). The hysteresis and kinetics are examined by galvanostatic intermittent titration technique (GITT). Clearly, the charge profiles of the less fluorinated samples display the high-voltage plateau with an over potential of 180 – 260 mV, which is greater than that (90 – 100 mV) in the low-voltage sloping region (**Figure 2d**). However, the high fluorination alters the high-voltage O reactions above 4.5 V, leading to improved kinetics and suppressed hysteresis (symmetric profiles). Therefore, the design principle of incorporating more F⁻ anion and Mn²⁺ cation is effective to enhance the cyclability while maintain a reasonably high reversible capacity.

2.3 Redox Contribution

Understanding the interplay between the cationic and anionic redox reactions is essential to underpin the electrochemical performance. We characterize the chemical states of cations and anions at different states of charge using the spectroscopic techniques based on resonant inelastic X-ray scattering (RIXS). **Figure 3a** shows the Mn *L*-edge inverse-partial fluorescence yield (iPFY) spectra extracted from the Mn *L*-edge RIXS maps, which is a non-distorted bulk probe of the Mn *3d* valence state directly.^[12] In comparison with Mn²⁺, Mn³⁺, and Mn⁴⁺ references, a large portion of Mn in the 1st cycle charged (4.8 V) samples is present at 4+ with some reduction. The

average Mn valence state at fully charged states is ~ 3.5 from Mn *L*-edge iPFY spectra (**Figure 3b** & **Figure S6a**), slightly lower than that (~ 3.75) from Mn *K*-edge X-ray absorption near-edge spectroscopy (XANES) (**Figure S5**), due to the relatively large contribution of the reduced surface Mn from iPFY spectra. As reported previously,^[9a, 11] Nb⁵⁺ remains inactive throughout the cycling, which is confirmed in one representative DRX sample, M_{0.60}F_{0.60} (**Figure S6b**). Given the Mn²⁺ at pristine state, the cationic Mn redox makes a significant contribution to the charge compensation in these DRX materials.

Figure 3c shows the O *K*-edge RIXS at pristine and the 1st 4.8 V charged state (1Ch.) collected at the excitation energy of 531 eV, which is the characteristic energy for fingerprinting the oxidized O state, i.e., O^{*n*-} ($0 < n < 2$), through a feature at the emission energy of ~ 523.5 eV in the Mn based systems (red arrows in **Figure 3d**).^[9d, 12] The weak shoulder and small contrast between the pristine (representative M_{0.60}F_{0.60} in **Figure S6c**) and charged electrodes at the ~ 523.5 eV emission energy here indicates that the lattice O redox reaction is minimal in all samples. This is further confirmed by the full-range O *K*-edge RIXS maps of the fully charged electrodes, as shown in **Figure 3d**, where the oxidized oxygen feature is very weak (red arrows) compared to the typical oxygen-redox systems.^[12-13]

To further evaluate the irreversible reaction of the oxidized oxygen, differential electrochemical mass spectrometry (DEMS) measurements were performed on M_{0.45}F_{0.15} and M_{0.625}F_{0.675} with the contrasting F content (**Figure 4**). The M_{0.45}F_{0.15} sample exhibits a small amount of oxygen evolution (1.67 mmol mol⁻¹, corresponding to 0.18% total O in M_{0.45}F_{0.15} sample) at the high voltage above 4.6 V, consistent with the minimal lattice oxygen redox in the Mn²⁺-based DRX samples. On the other hand, no oxygen gas release is detected throughout the

first cycle of the $M_{0.625}F_{0.675}$ sample, indicating the oxygen oxidation reaction is indeed suppressed at high fluorination. Moreover, a small amount of CO_2 gas release occurs in both samples, which might be related to the electrolyte decomposition and/or surface carbonate contamination from the material preparation.^[9a]

2.4 Charge Mechanism at High F Substitution

A detailed characterization was performed on $Li_{1.2}Mn_{0.6}Nb_{0.2}O_{1.4}F_{0.6}$ ($M_{0.60}F_{0.60}$) sample to investigate the cationic charge compensation mechanism. The Mn *L*-edge RIXS-iPFY spectra (**Figure 5a**) are collected at different states of charge during the 1st cycle (pristine, C4.3, C4.8, D3.7, D2.8, and D1.5). From the Mn *L*-edge RIXS-iPFY results, upon charging, most Mn^{2+} oxidation takes place below 4.3 V (C4.3), with a slight oxidation occurring from 4.3 to 4.8 V charge. During discharge, Mn^{4+}/Mn^{3+} reduction mainly occurs above 2.8 V (D2.8), followed by almost full reduction to Mn^{2+} till 1.5 V discharge (D1.5). The quantified cationic redox processes based on Mn *L*-edge RIXS-iPFY are summarized in **Figure 5b**. Most Mn oxidation occurs before 4.3 V charge, where Mn ends up with mixed Mn^{3+} (59%) and Mn^{4+} (33%). Charge compensation above 4.3 V is dominated by Mn^{3+} to Mn^{4+} oxidation (~10%). During discharge, reduction of Mn^{4+} completes above 2.8 V (50% Mn^{3+} and 50% Mn^{2+}) and Mn^{3+} gets further reduced to Mn^{2+} below 2.8 V. We note that, even without the quantitative analysis, the spectral lineshape of the discharged state shows directly the dominating Mn^{2+} state compared with the reference spectra.

2.5 Cycling Performance at High Fluorination

To examine the reversibility of redox processes upon cycling, the highly fluorinated $M_{0.60}F_{0.60}$ cathode is charged to different cutoff potentials. As shown in the dQ/dV plots (**Figure 6a**), the

charge process is characterized by consecutive oxidation reactions before 4.3 V, while the reduction processes are more distinguishable during discharge. When charged to 3.8 V, the most distinct discharge feature is the reduction peak around 3.3 V. When progressively increasing charge cutoff voltage, the reduction reaction starts at a higher potential and continues to evolve in the medium voltage range, resulting in an ever increasing reduction peak centered on 3.3 V. Similarly, the low-voltage region is featured by a reduction peak around 2.4 V. According to the Mn *L*-edge RIXS (**Figure 5a**), the reduction peaks around 3.3 and 2.4 V should be associated with the Mn⁴⁺/Mn³⁺ and Mn³⁺/Mn²⁺ redox. The Mn⁴⁺/Mn³⁺ redox reaction in the Mn²⁺-based DRX cathode is similar to that in the Mn³⁺-based one.^[11] The reversibility of both cationic Mn redox reactions is revealed when cycled within different voltage ranges (**Figure 6b-f** & **Figure 7a**). At the charge cutoff voltage below 4.5 V, the charge and discharge processes mostly remain unchanged. When increasing the cutoff voltage to 4.8 V, the Mn³⁺/Mn²⁺ redox gradually increases at the expense of Mn⁴⁺/Mn³⁺ redox (**Figure 6f**). The decreased Mn⁴⁺ upon 4.8 V cycling could be attributed to the parasitic reaction related to the electrolyte decomposition, as evidenced by the large polarization at 4.8 V cycling (**Figure 7b, c**). Therefore, the highly fluorinated samples, M_{0.60}F_{0.60} and M_{0.625}F_{0.675}, are subjected to the long-term cycling within the range of 4.5 – 1.5 V at a high rate of C/3 after the full activation of all redox processes between 4.8 and 1.5 V during the first two cycles. At a current density of 100 mA g⁻¹, M_{0.60}F_{0.60} and M_{0.625}F_{0.675} samples exhibit an initial capacity of 197 and 177 mAh g⁻¹, with a capacity retention of 73.5% and 84.8%, respectively, after 100 cycles (**Figure 7d**).

3. Discussion

Design of cathode materials with robust structure and reversible redox centers is the key to achieve the goal of high capacity and stable cycling. The DRX structure largely removes the constraint on TM redox centers (e.g., Ni, Mn, Fe) that can form the desired phase with the appropriate d^0 metal, of which the $\text{Mn}^{2+}/\text{Mn}^{4+}$ redox reactions offer doubled capacity per TM. The electrochemical performance of DRX cathodes is strongly correlated with multiple factors: Li content, Li to active metal ratio, and choice of TMs. In general, more Li content leads to a higher theoretical capacity with the possible anionic O redox enabled by the Li-O-Li configuration. However, anionic O redox often triggers irreversible reactions at high voltages. So an optimal Li content is important to facilitate the Li^+ percolation and incorporate more low-valence redox active TM, while reducing the high-valence inactive TM.

Herein, $\text{Li}_{1.2}\text{Mn}_{0.4+z/3}\text{Nb}_{0.4-z/3}\text{O}_{2-z}\text{F}_z$ with the fixed 1.2 Li ensures the effective Li^+ percolation and accommodates more double $\text{Mn}^{2+/4+}$ redox through the incorporation of pentavalent Nb and F substitution. The full utilization of $\text{Mn}^{2+}/\text{Mn}^{4+}$ redox would compensate for the total Li in $\text{Li}_{1.2}\text{Mn}_{0.6}\text{Nb}_{0.2}\text{O}_{1.4}\text{F}_{0.6}$ ($\text{M}_{0.60}\text{F}_{0.60}$). However, our detailed analysis shows that it is difficult to achieve a full use of $\text{Mn}^{2+}/\text{Mn}^{4+}$ redox. This could be related to the local environment around Li in the cubic lattice as the mobility of Li^+ may vary when it is surrounded by more electronegative F. Additionally, it is difficult to achieve high fluorination in the bulk lattice, as evidenced by the longer milling time needed for highly fluorinated DRX sample.

It is worth noting that these DRX materials prepared by extensive milling have poor crystallinity, especially at the surface. As such, the parasitic reactions are inevitable in these materials when they are subjected to high-voltage cycling. However, the cycling performance demonstrated in this work is very promising towards the dominating redox chemistry of $\text{Mn}^{2+}/\text{Mn}^{4+}$, given the minimal control in material properties. Particularly,

$\text{Li}_{1.2}\text{Mn}_{0.625}\text{Nb}_{0.175}\text{O}_{1.325}\text{F}_{0.675}$ ($\text{M}_{0.625}\text{F}_{0.675}$) sample demonstrates quite stable cycling at a capacity of $\sim 170 \text{ mAh g}^{-1}$ at a high rate of C/3 (100 mA g^{-1}), suggesting the rate capability is not a barrier for the practical use of DRX cathode. Moreover, the large capacity decay above 4.5 V cycling suggests the challenge of high-voltage electrolyte remains formidable, even for the reversible use of $\text{Mn}^{2+}/\text{Mn}^{4+}$ redox.

4. Conclusion

In this work, a series of fluorinated DRX compounds based on $\text{Mn}^{2+}\text{-Nb}^{5+}$ combination, $\text{Li}_{1.2}\text{Mn}_{0.4+z/3}\text{Nb}_{0.4-z/3}\text{O}_{2-z}\text{F}_z$, have been designed and synthesized via a mechanochemical reaction. The as-produced materials deliver an initial capacity of 250 – 300 mAh g^{-1} . Incorporating F in the DRX lattice results in a slight decrease in the reversible capacity, but it remains practically high, with much improved capacity retention, less polarization and smaller hysteresis. Cationic $\text{Mn}^{2+}/\text{Mn}^{4+}$ redox is the dominating charge compensation mechanism in highly fluorinated samples. More importantly, $\text{Mn}^{2+}/\text{Mn}^{4+}$ redox exhibits an excellent reversibility at a practical rate. This work not only demonstrates a rational design of DRX materials to tailor the stoichiometry and manipulate the key redox reactions, but also showcases the possible utilization of DRX cathodes towards the practical applications.

5. Experimental Section

Synthesis and Physical Characterization: $\text{Li}_{1.2}\text{Mn}_{0.4+z/3}\text{Nb}_{0.4-z/3}\text{O}_{2-z}\text{F}_z$ compounds were synthesized via a mechanochemical reaction. Oxides of Li_2O (10% Li excess), MnO and Nb_2O_5 as well as LiF were used as the precursors. The stoichiometric amounts of precursors were loaded into a milling jar in an Ar-filled glovebox, then subjected to mechanical milling for the designated durations until pure DRX phase was obtained. The milled powder was then collected in an Ar-filled glove box. XRD patterns were obtained on a Bruker D2-Phaser with $\text{Cu K}\alpha$

radiation ($\lambda = 1.54178 \text{ \AA}$) and analyzed by conventional Rietveld refinement method using general structure analysis system package with the graphical user interface (EXPGUI).^[14] Scanning electron microscopy (SEM) images were collected on a JEOL JSM-7000F with an EDS detector.

Electrochemical Characterization: The as-prepared $\text{Li}_{1.2}\text{Mn}_{0.4+z/3}\text{Nb}_{0.4-z/3}\text{O}_{2-z}\text{F}_z$ powder was first mixed with carbon black to improve the electrical conductivity of the composite electrode. The carbon-processed $\text{Li}_{1.2}\text{Mn}_{0.4+z/3}\text{Nb}_{0.4-z/3}\text{O}_{2-z}\text{F}_z$ powder was then mixed with polyvinylidene fluoride (PVdF, 6 wt%) dissolved into N-methylpyrrolidone solvent, and the slurry was cast on an aluminum foil (20 μm thickness) using a doctor blade. The cast slurry was dried under vacuum at 120 °C for 12 h. The punched electrode was used as the cathode along with Li metal, separator (Celgard 2400), and electrolyte (1 M LiPF_6 in 1:2 w/w ethylene carbonate–diethyl carbonate) to assemble the coin cells in an Ar-filled glovebox. GITT test was conducted by resting the cells after charge/discharge at C/20 for 30 min. The mass loading of active materials was $\sim 2.5 \text{ mg cm}^{-2}$. 1 C capacity was defined as the theoretical capacity based on 1 Li^+ .

Ex situ XAS and RIXS: Mn L-edge and O K-edge RIXS along with O K-edge soft XAS were carried out at ultra-high efficiency iRIXS endstation at Beamline 8.0.1 at the Advanced Light Sources (ALS). All the cycled electrodes were immediately removed from the coin cells at designated states of charge in an Ar-filled glovebox. The harvested electrodes were then rinsed by dimethyl carbonate solvent to remove surface species inside the glovebox. All dried electrodes were transferred into the experimental vacuum chamber using a specially designed sample transfer kit in an Ar-filled glove box to avoid air exposure. Sample surface was mounted 45° to the incident beam, and the outgoing photon direction along the RIXS spectrograph is 90°. The resolution of the excitation

energy and emission energy is about 0.2 and 0.3 eV, respectively. An excitation energy step size of 0.2 eV was chosen for all RIXS maps. All other technical details on RIXS data analysis, especially the Mn-*L* quantifications, can be found in the previous report.^[12] O *K*-edge sXAS were collected TFY mode of each cycled electrode. The experimental energy resolution was 0.15 eV without considering core-hole lifetime broadening. All the XAS and RIXS data were normalized to the beam flux measured by the upstream gold mesh, and RIXS spectra were further normalized by the data collection time.

Ex situ XANES: Mn and Nb *K*-edge XANES were performed at beamline 2-2 at Stanford Synchrotron Radiation Lightsource. Each cycled electrode was sandwiched between two Kapton films in an Ar-filled glovebox and a Si (220) crystal was applied as a monochromator. Higher harmonics were eliminated via detuning the monochromator by 50% at the *K*-edge during data collection. Monochromatic energy calibration was accomplished by the E_0 value of 6539 and 18986 eV for Mn and Nb metal foil reference, respectively. The data processing of XANES spectra was conducted using Athena software.

DEMS: The evolution of CO₂ and O₂ gas was investigated using DEMS. The cathodes used in DEMS experiments were fabricated by mixing the carbon-processed powder with polytetrafluoroethylene binder and subsequently pressing the mixture onto a stainless-steel mesh current collector. These cathodes were used along with Li metal, separator (one sheet of Whatman quartz microfiber filter paper on the anode side and one sheet of Celgard 2500 on the cathode side), and electrolyte (1M LiPF₆ in 1:1 vol/vol ethylene carbonate-diethyl carbonate) to assemble customized Swagelok type cells in an Ar atmosphere glovebox. The hermetically sealed cells were appropriately attached to the DEMS apparatus to avoid air exposure. The DEMS cell was initially rested at the open circuit voltage for 3 h and charge/discharge was

conducted (C/10, 4.8 – 1.5 V) with galvanostatic control using a BioLogic SP-300 potentiostat under a positive Ar pressure (~1.2 bar). Meanwhile, gas evolution was monitored using a custom-built DEMS apparatus. Throughout the experiment, the cell headspace was swept every 10 minutes and any accumulated gases were swept to the mass spectrometer chamber for analysis. The DEMS apparatus is calibrated for O₂ and CO₂ in Ar, allowing for the determination of the partial pressures of each analyte. The amount of each gas evolved was then quantified using the temperature and volume of the gas sample. The customized Swagelok cells and DEMS apparatus are both described in greater detail in a previous report.^[15]

Acknowledgements

This work is supported by the Assistant Secretary for Energy Efficiency and Renewable Energy, Office of Vehicle Technologies of the U.S. Department of Energy under Contract No. DE-AC02-05CH11231. Use of the Advanced Light Source is supported by the Office of Science, Office of Basic Energy Sciences, of the US Department of Energy under contract No. DE-AC02-05CH11231. Use of resources at the Molecular Foundry was supported by the Office of Science, Office of Basic Energy Sciences, of the U.S. Department of Energy under Contract No. DE-AC02-05CH11231. Use of the Stanford Synchrotron Radiation Lightsource, SLAC National Accelerator Laboratory, is supported by the U.S. Department of Energy, Office of Science, Office of Basic Energy Sciences under Contract No. DE-AC02-76SF00515.

Conflict of Interest

The authors declare no conflict of interest.

Keywords

Li-ion batteries, cathode materials, cation-disordered rocksalt, double redox, anionic oxygen redox

References

- [1] a) M. S. Whittingham, *Chem. Rev.* **2004**, *104*, 4271; b) J. B. Goodenough, Y. Kim, *Chem. Mater.* **2009**, *22*, 587; c) J. Xu, F. Lin, M. M. Doeff, W. Tong, *J. Mater. Chem. A* **2017**, *5*, 874.
- [2] a) A. Urban, J. Lee, G. Ceder, *Adv. Energy Mater.* **2014**, *4*, 1400478; b) R. Clément, Z. Lun, G. Ceder, *Energy Environ. Sci.* **2020**, *13*, 345.
- [3] A. Urban, I. Matts, A. Abdellahi, G. Ceder, *Adv. Energy Mater.* **2016**, *6*, 1600488.
- [4] a) N. Yabuuchi, M. Takeuchi, M. Nakayama, H. Shiiba, M. Ogawa, K. Nakayama, T. Ohta, D. Endo, T. Ozaki, T. Inamasu, *PANS* **2015**, *112*, 7650; b) D.-H. Seo, J. Lee, A. Urban, R. Malik, S. Kang, G. Ceder, *Nat. Chem.* **2016**, *8*, 692; c) A. Kitajou, K. Tanaka, H. Miki, H. Koga, T. Okajima, S. Okada, *Electrochemistry* **2016**, *84*, 597; d) N. Yabuuchi, M. Takeuchi, S. Komaba, S. Ichikawa, T. Ozaki, T. Inamasu, *Chem. Commun.* **2016**, *52*, 2051; e) Y. Kobayashi, M. Sawamura, S. Kondo, M. Harada, Y. Noda, M. Nakayama, S. Kobayakawa, W. Zhao, A. Nakao, A. Yasui, H. B. Rajendra, K. Yamanaka, T. Ohta, N. Yabuuchi, *Mater. Today* **2020**; f) N. Takeda, S. Hoshino, L. Xie, S. Chen, I. Ikeuchi, R. Natsui, K. Nakura, N. Yabuuchi, *J. Power Sources* **2017**, *367*, 122; g) N. Takeda, I. Ikeuchi, R. Natsui, K. Nakura, N. Yabuuchi, *ACS Appl. Energy Mater.* **2019**, *2*, 1629; h) N. Yabuuchi, Y. Tahara, S. Komaba, S. Kitada, Y. Kajiya, *Chem. Mater.* **2016**, *28*, 416.
- [5] a) S. L. Glazier, J. Li, J. Zhou, T. Bond, J. Dahn, *Chem. Mater.* **2015**, *27*, 7751; b) G. Assat, D. Foix, C. Delacourt, A. Iadecola, R. Dedryvère, J.-M. Tarascon, *Nat. Commun.* **2017**, *8*, 2219; c) G. Assat, A. Iadecola, C. Delacourt, R. m. Dedryvère, J.-M. Tarascon, *Chem. Mater.* **2017**, *29*, 9714; d) W. E. Gent, K. Lim, Y. Liang, Q. Li, T. Barnes, S.-J. Ahn, K. H. Stone, M. McIntire, J. Hong, J. H. Song, *Nat. Commun.* **2017**, *8*, 2091; e) M. M. Thackeray, S.-H. Kang, C. S. Johnson,

J. T. Vaughey, R. Benedek, S. Hackney, *J. Mater. Chem.* **2007**, *17*, 3112; f) G. Assat, C. Delacourt, D. A. D. Corte, J.-M. Tarascon, *J. Electrochem. Soc.* **2016**, *163*, A2965; g) Q. Jacquet, A. Iadecola, M. Saubanère, H. Li, E. J. Berg, G. Rousse, J. Cabana, M.-L. Doublet, J.-M. Tarascon, *J. Am. Chem. Soc.* **2019**, *141*, 11452; h) A. Grimaud, W. T. Hong, Y. Shao-Horn, J. M. Tarascon, *Nat. Mater.* **2016**, *15*, 121; i) N. Li, S. Hwang, M. Sun, Y. Fu, V. S. Battaglia, D. Su, W. Tong, *Adv. Energy Mater.* **2019**, *9*, 1902258; j) N. Li, S. Sallis, J. K. Papp, J. Wei, B. D. McCloskey, W. Yang, W. Tong, *ACS Energy Lett.* **2019**, *4*, 2836; k) J. Xu, M. Sun, R. Qiao, S. E. Renfrew, L. Ma, T. Wu, S. Hwang, D. Nordlund, D. Su, K. Amine, J. Lu, B. D. McCloskey, W. Yang, W. Tong, *Nat. Commun.* **2018**, *9*, 947.

[6] a) J. Lee, D.-H. Seo, M. Balasubramanian, N. Twu, X. Li, G. Ceder, *Energy Environ. Sci.* **2015**, *8*, 3255; b) R. Wang, X. Li, L. Liu, J. Lee, D.-H. Seo, S.-H. Bo, A. Urban, G. Ceder, *Electrochem. Commun.* **2015**, *60*, 70; c) N. Yabuuchi, M. Nakayama, M. Takeuchi, S. Komaba, Y. Hashimoto, T. Mukai, H. Shiiba, K. Sato, Y. Kobayashi, A. Nakao, *Nat. Commun.* **2016**, *7*, 13814; d) W. H. Kan, D. Chen, J. K. Papp, A. K. Shukla, A. Huq, C. M. Brown, B. D. McCloskey, G. Chen, *Chem. Mater.* **2018**, *30*, 1655; e) Z. Yu, X. Qu, A. Dou, M. Su, Y. Liu, F. Wu, *ACS Appl. Mater. Interfaces* **2019**; f) S. Zheng, D. Liu, L. Tao, X. Fan, K. Liu, G. Liang, A. Dou, M. Su, Y. Liu, D. Chu, *J. Alloys Compd.* **2019**, *773*, 1; g) D. Chen, W. H. Kan, G. Chen, *Adv. Energy Mater.* **2019**, *9*, 1901255.

[7] a) W. D. Richards, S. T. Dacek, D. A. Kitchaev, G. Ceder, *Adv. Energy Mater.* **2018**, *8*, 1701533; b) Z. Lun, B. Ouyang, Z. Cai, R. J. Clément, D.-H. Kwon, J. Huang, J. K. Papp, M. Balasubramanian, Y. Tian, B. D. McCloskey, H. Ji, H. Kim, D. Kitchaev, G. Ceder, *Chem* **2020**, *6*, 153; c) J. Lee, J. K. Papp, R. J. Clément, S. Sallis, D.-H. Kwon, T. Shi, W. Yang, B. D.

- McCloskey, G. Ceder, *Nat. Commun.* **2017**, *8*, 981; d) M. J. Crafton, Y. Yue, T.-Y. Huang, W. Tong, B. D. McCloskey, *Adv. Energy Mater.* **2020**, *10*, 2001500.
- [8] M. A. Cambaz, B. P. Vinayan, H. Geßwein, A. Schiele, A. Sarapulova, T. Diemant, A. Mazilkin, T. Brezesinski, R. J. Behm, H. Ehrenberg, *Chem. Mater.* **2019**, *31*, 4330.
- [9] a) J. Lee, D. A. Kitchaev, D.-H. Kwon, C.-W. Lee, J. K. Papp, Y.-S. Liu, Z. Lun, R. J. Clément, T. Shi, B. D. McCloskey, J. Guo, M. Balasubramanian, G. Ceder, *Nature* **2018**, 556, 185; b) J. Xu, S. Renfrew, M. A. Marcus, M. Sun, B. D. McCloskey, W. Tong, *J. Phys. Chem. C* **2017**, *121*, 11100; c) H. Ji, D. A. Kitchaev, Z. Lun, H. Kim, E. Foley, D.-H. Kwon, Y. Tian, M. Balasubramanian, M. Bianchini, Z. Cai, R. J. Clément, J. C. Kim, G. Ceder, *Chem. Mater.* **2019**, *31*, 2431; d) E. Zhao, Q. Li, F. Meng, J. Liu, J. Wang, L. He, Z. Jiang, Q. Zhang, X. Yu, L. Gu, W. Yang, H. Li, F. Wang, X. Huang, *Angew. Chem. Int. Edit.* **2019**, *58*, 4323; e) H. Li, M. Cormier, N. Zhang, J. Inglis, J. Li, J. Dahn, *J. Electrochem. Soc.* **2019**, *166*, A429; f) A. Abdellahi, A. Urban, S. Dacek, G. Ceder, *Chem. Mater.* **2016**, *28*, 3659.
- [10] R. J. Clément, D. Kitchaev, J. Lee, G. Ceder, *Chem. Mater.* **2018**, *30*, 6945.
- [11] Y. Yue, N. Li, L. Li, E. E. Foley, Y. Fu, V. S. Battaglia, R. J. Clément, C. Wang, W. Tong, *Chem. Mater.* **2020**, *32*, 4490.
- [12] K. Dai, J. Wu, Z. Zhuo, Q. Li, S. Sallis, J. Mao, G. Ai, C. Sun, Z. Li, W. E. Gent, W. C. Chueh, Y.-d. Chuang, R. Zeng, Z.-x. Shen, F. Pan, S. Yan, L. F. J. Piper, Z. Hussain, G. Liu, W. Yang, *Joule* **2019**, *3*, 518.
- [13] a) A. van Bommel, L. Krause, J. Dahn, *J. Electrochem. Soc.* **2011**, *158*, A731; b) D. Eum, B. Kim, S. J. Kim, H. Park, J. Wu, S.-P. Cho, G. Yoon, M. H. Lee, S.-K. Jung, W. Yang, W. M. Seong, K. Ku, O. Tamwattaba, S. K. Park, I. Hwang, K. Kang, *Nat. Mater.* **2020**, *19*, 419.

[14] B. H. Toby, *J. Appl. Crystallogr.* **2001**, *34*, 210.

[15] B. D. McCloskey, D. S. Bethune, R. M. Shelby, G. Girishkumar, A. C. Luntz, *J. Phys. Chem. Lett.* **2011**, *2*, 1161.

Supplementary Information

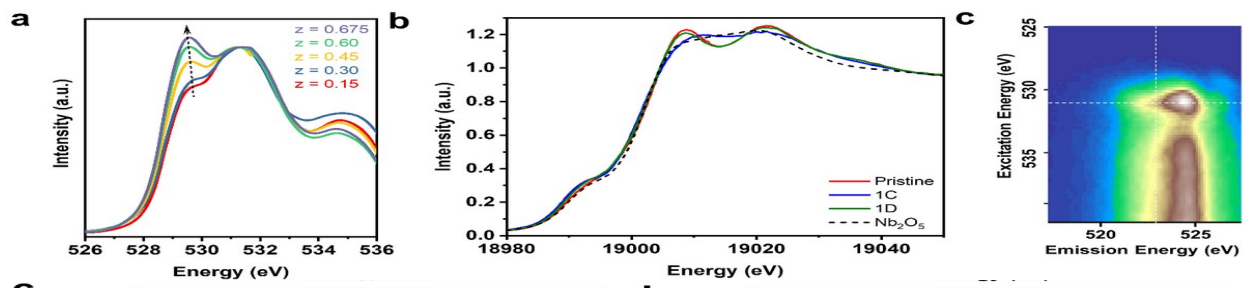


Figure S6. (a) O K-edge XAS of $\text{Li}_{1.2}\text{Mn}_{0.4+z/3}\text{Nb}_{0.4-z/3}\text{O}_{2-z}\text{F}_z$ samples at 1st 4.8 V charge (1C) state, showing Mn^{4+} -O hybridization increases with F content. (b) Nb K-edge XANES of one representative DRX sample, $\text{M}_{0.60}\text{F}_{0.60}$, at pristine, 1st 4.8 V charge (1C), and 1st 1.5 V discharge (1D) states, showing Nb^{5+} is inactive during electrochemical cycling. (c) O K-edge RIXS map of one representative DRX sample, $\text{M}_{0.60}\text{F}_{0.60}$, showing no O redox feature at pristine state, as guided by the white dash lines at 531 eV excitation energy and 523 eV emission energy.

Table S1. The refined structural parameters of DRX cathodes, $\text{Li}_{1.2}\text{Mn}_{0.4+z/3}\text{Nb}_{0.4-z/3}\text{O}_{2-z}\text{F}_z$, based on*Fm* $\bar{3}$ *m* space group.

Material	$\text{M}_{0.45}\text{F}_{0.15}$	$\text{M}_{0.50}\text{F}_{0.30}$	$\text{M}_{0.55}\text{F}_{0.45}$	$\text{M}_{0.60}\text{F}_{0.60}$	$\text{M}_{0.625}\text{F}_{0.675}$
a [Å]	4.259(6)	4.255(5)	4.253(8)	4.252(8)	4.251(3)
V [Å ³]	77.253(3)	77.059(2)	76.928(3)	76.874(1)	76.820(8)
Refined R_p [%]	1.51	1.18	1.13	0.97	0.95
Site 4a (x, y, z) = (0, 0, 0)	Li(1) occupancy	0.6000	0.6000	0.6000	0.6000
	Mn(1) occupancy	0.2250	0.2500	0.2750	0.3125
	Nb(1) occupancy	0.1750	0.1500	0.1250	0.0875
Site 4a (x, y, z) = (0.5, 0.5, 0.5)	O(1) occupancy	0.9250	0.8500	0.7750	0.7000
	F(1) occupancy	0.0750	0.1500	0.2250	0.3375